University of Groningen

The diversity and similarity of simulated cold dark matter haloes

Navarro, Julio F.; Ludlow, Aaron; Springel, Volker; Wang, Jie; Vogelsberger, Mark; White, Simon D. M.; Jenkins, Adrian; Frenk, Carlos S.; Helmi, Amina

IMPORTANT NOTE: You are advised to consult the publisher's version (publisher's PDF) if you wish to cite from it. Please check the document version below.

Document Version
Publisher's PDF, also known as Version of record

[Link to publication in University of Groningen/UMCG research database](#)

The diversity and similarity of simulated cold dark matter haloes

Julio F. Navarro,[1,2]★ Aaron Ludlow,[1] Volker Springel,[3] Jie Wang,[3] Mark Vogelsberger,[3] Simon D. M. White,[3] Adrian Jenkins,[4] Carlos S. Frenk[4] and Amina Helmi[5]

[1]*Department of Physics and Astronomy, University of Victoria, Victoria, BC, V8P 5C2, Canada*
[2]*Department of Astronomy, University of Massachusetts, Amherst, MA 01003-9305, USA*
[3]*Max-Planck-Institut für Astrophysik, Karl-Schwarzschild-Straße 1, 85740 Garching bei München, Germany*
[4]*Institute for Computational Cosmology, Department of Physics, University of Durham, South Road, Durham DH1 3LE*
[5]*Kapteyn Astronomical Institute, University of Groningen, PO Box 800, 9700 AV Groningen, the Netherlands*

ABSTRACT

We study the mass, velocity dispersion and anisotropy profiles of Λ cold dark matter (ΛCDM) haloes using a suite of *N*-body simulations of unprecedented numerical resolution. The *Aquarius Project* follows the formation of six different galaxy-sized haloes simulated several times at varying numerical resolution, allowing numerical convergence to be assessed directly. The highest resolution simulation represents a single dark matter halo using 4.4 *billion* particles, of which 1.1 billion end up within the virial radius. Our analysis confirms a number of results claimed by earlier work, and clarifies a few issues where conflicting claims may be found in the recent literature. The mass profile of ΛCDM haloes deviates slightly but systematically from the form proposed by Navarro, Frenk & White. The spherically averaged density profile becomes progressively shallower inwards and, at the innermost resolved radius, the logarithmic slope is $\gamma \equiv -d \ln \rho / d \ln r \lesssim 1$. Asymptotic inner slopes as steep as the recently claimed $\rho \propto r^{-1.2}$ are clearly ruled out. The radial dependence of γ is well approximated by a power law, $\gamma \propto r^{\alpha}$ (the Einasto profile). The shape parameter, α, varies slightly but significantly from halo to halo, implying that the mass profiles of ΛCDM haloes are not strictly universal: different haloes cannot, in general, be rescaled to look identical. Departures from similarity are also seen in velocity dispersion profiles and correlate with those in density profiles so as to preserve a power-law form for the spherically averaged pseudo-phase-space density, $\rho/\sigma^3 \propto r^{-1.875}$. The index here is identical to that of Bertschinger's similarity solution for self-similar infall on to a point mass from an otherwise uniform Einstein–de Sitter universe. The origin of this striking behaviour is unclear, but its robustness suggests that it reflects a fundamental structural property of ΛCDM haloes. Our conclusions are reliable down to radii below 0.4 per cent of the virial radius, providing well-defined predictions for halo structure when baryonic effects are neglected, and thus an instructive theoretical template against which the modifications induced by the baryonic components of real galaxies can be judged.

Key words: methods: numerical – dark matter.

1 INTRODUCTION

A couple of decades of steady progress in the simulation of non-linear structures in a cold dark matter (CDM) dominated universe have resulted in significant advances in our understanding of the clustering of dark matter on the scale of galactic haloes. There is now widespread consensus that the hierarchical assembly of CDM haloes yields (1) mass profiles that are approximately 'universal' (i.e. independent of mass and cosmological parameters aside from simple physical scalings (Navarro, Frenk & White 1996, 1997, hereafter NFW), (2) strongly triaxial shapes, with a slight preference for nearly prolate systems (e.g. Frenk et al. 1988; Jing & Suto 2002; Allgood et al. 2006; Hayashi, Navarro & Springel 2007), (3) abundant, but non-dominant, substructure (Klypin et al. 1999; Moore et al. 1999a; Ghigna et al. 2000; Gao et al. 2004) and (4) 'cuspy' inner mass profiles, where the central density increases systematically as the numerical resolution of the calculation is improved

★E-mail: jfn@uvic.ca

(see e.g. NFW; Moore et al. 1999b, hereafter M99; Fukushige & Makino 2001; Navarro et al. 2004; Diemand et al. 2005).

Despite this consensus, there are a number of issues where conflicting claims may be found in the recent literature, hindering the design and interpretation of observational tests aimed at validating or ruling out various aspects of the CDM theory on these scales. One contentious issue concerns the statistics, spatial distribution and structure of substructure, and their consequences for the discovery and interpretation of possible signals of dark matter annihilation in the gamma-ray sky (Stoehr et al. 2003; Diemand, Kuhlen & Madau 2007; Kuhlen, Diemand & Madau 2008; Springel et al. 2008b and references therein). The controversy extends to the structure of the inner cusps both of the main halo and of substructure haloes, where some recent work has claimed a well-defined central slope of $\rho \propto r^{-1.2}$ (Diemand, Moore & Stadel 2004; Diemand et al. 2005, 2008) whereas others have argued that no compelling evidence for such power-law behaviour is apparent (Navarro et al. 2004; Graham et al. 2006).

Considerable debate also surrounds whether the structure of CDM haloes is truly 'universal'. This is indeed the case if haloes have mass profiles that are well described by two-parameter formulae, such as the NFW profile or some of its modifications (see e.g. M99). These profiles have two scaling parameters (mass and size) but fixed *shape*, so that two different haloes can, in principle, be rescaled to be indistinguishable from each other.

On the other hand, recent work suggests that at least *three* parameters may be needed to describe halo mass profiles accurately. An example is the Einasto formula (Einasto 1965), shown by Navarro et al. (2004) to significantly improve the accuracy of the fits to the inner density profiles of simulated haloes. It is unclear from that work, however, whether the improvement is due to the fact that the Einasto formula has a different asymptotic inner behaviour than NFW or to the extra shape parameter it introduces. Merritt et al. (2005, 2006) explored this further and argued that the third parameter is indeed needed to account faithfully for the curvature in the shape of the density profile. Merritt et al.'s conclusions have received support from the work of Gao et al. (2008) and Hayashi & White (2008), who have stacked density profiles of many haloes of similar mass to show that mean profile shape and, in particular, the Einasto shape parameter α (see equation 4) depend systematically on halo mass. This implies that the mass profile of ΛCDM haloes is not strictly universal; no simple scaling of the average profile of cluster haloes will provide an accurate fit to the average profile of galaxy haloes.

Many of these controversies and uncertainties may be traced to the fact that earlier work has lacked the numerical resolution and the representative halo sample needed to settle the debate. For example, the dark matter annihilation flux observable from the Earth depends crucially on resolving not only substructures but also the nested 'substructure within substructure' expected from the hierarchical assembly of CDM haloes. Only the most recent simulations have been able to begin addressing this issue (see e.g. Diemand et al. 2008; Springel et al. 2008a,b).

A similar comment applies to the structure of the inner cusp, where pinning down the asymptotic inner behaviour of the dark matter density profile depends crucially on understanding the limitations introduced by, for example, finite particle number, gravitational softening and time-stepping technique.

We have shown in earlier work (Power et al. 2003, hereafter P03) that, when suitable choices of the numerical parameters are made, the main factor determining the innermost radius where the mass profile may be measured reliably is the total number of particles used in the simulation. Empirically, the boundary of the region where numerical convergence is achieved roughly corresponds to the radius where the two-body relaxation time, $t_{\rm relax}$, exceeds the age of the Universe. Since $t_{\rm relax}$ scales roughly like the enclosed number of particles times the local orbital time-scale, and the latter drops sharply towards the centre, extending the resolved region inwards even modestly requires a dramatic increase in the total number of particles.

These difficulties, coupled to the significant halo-to-halo scatter already seen in early work, imply that substantive progress on these issues requires a concerted numerical effort where *several* different haloes are simulated with *varying numerical resolution*, so that cosmic variance and numerical convergence may be assessed directly.

These are the aims of *The Aquarius Project*, a recently completed suite of numerical simulations of the formation of galaxy-sized haloes in the ΛCDM cosmogony. The series includes resimulations of six different $\sim 10^{12}\,{\rm M}_\odot$ haloes where the number of particles is systematically varied. In one case, the *same* halo is simulated five times, gradually increasing the number of particles in the halo from about 1 million to ~ 1.1 *billion* within the virial radius. The highest resolution simulations of the other five haloes have roughly 100–200 million particles each within the virialized region.

The simulation series has been presented recently by Springel et al. (2008a,b), where the interested reader may find relevant details. Our first paper (Springel et al. 2008b) deals with predictions of the annihilation signal, whereas the second (Springel et al. 2008a) addresses the statistics, spatial distribution and structure of dark matter substructures. Here we deal with the structure of the *main halo*, with special emphasis on the structure of the inner cusp. The plan of this paper is as follows. Section 2 briefly summarizes the numerical parameters of our simulations; Sections 3 and 4 present our main results. We conclude with a brief discussion and summary in Section 5.

2 THE NUMERICAL SIMULATIONS

We present here for completeness a brief summary of the numerical simulations, and refer the reader to Springel et al. (2008a,b) for further details.

2.1 The cosmological parameters

All our simulations assume a ΛCDM cosmogony with the following parameters: $\Omega_{\rm m} = 0.25$, $\Omega_\Lambda = 0.75$, $\sigma_8 = 0.9$, $n_{\rm s} = 1$ and Hubble constant $H_0 = 100\,h\,{\rm km\,s^{-1}\,Mpc^{-1}} = 73\,{\rm km\,s^{-1}\,Mpc^{-1}}$. These cosmological parameters are the same adopted in previous numerical work by our group, such as the Millennium Simulation of Springel et al. (2005), and are consistent, within their uncertainties, with constraints derived from the *Wilkinson Microwave Anisotropy Probe* 1- and 5-year data analyses (Spergel et al. 2003; Komatsu et al. 2009) and with the recent cluster abundance analysis of Henry et al. (2009).

2.2 The code

The simulations were carried out with a new version of the GADGET (Springel, Yoshida & White 2001; Springel 2005) parallel cosmological code. This version, which we call GADGET-3, has been especially developed for this project, and implements a novel domain decomposition technique in order to achieve unprecedented dynamic range in massively parallel computer systems without sacrificing

Table 1. Basic parameters of the Aquarius simulations. We have simulated six different haloes, each at several different numerical resolutions.

Halo	m_p (M$_\odot$ h^{-1})	ϵ_G (pc h^{-1})	r_{200} (kpc h^{-1})	M_{200} (M$_\odot$ h^{-1})	N_{200} (10^6)	V_{max} (km s^{-1})	r_{max} (kpc h^{-1})	σ_{host} (km s^{-1})	σ_{max} (km s^{-1})
Aq-A-1	1.250×10^3	14	179.41	1.343×10^{12}	1074.06	208.75	20.69	117.47	261.70
Aq-A-2	1.000×10^4	48	179.49	1.345×10^{12}	134.47	208.49	20.54	117.13	261.88
Aq-A-3	3.585×10^4	87	179.31	1.341×10^{12}	37.39	209.22	20.35	117.31	262.80
Aq-A-4	2.868×10^5	250	179.36	1.342×10^{12}	4.68	209.24	20.58	117.23	262.29
Aq-A-5	2.294×10^6	500	180.05	1.357×10^{12}	0.59	209.17	20.84	116.61	260.59
Aq-B-2	4.706×10^3	48	137.02	5.982×10^{11}	127.09	157.68	29.31	89.59	190.74
Aq-C-2	1.021×10^4	48	177.26	1.295×10^{12}	126.77	222.40	23.70	124.08	270.50
Aq-D-2	1.020×10^4	48	177.28	1.295×10^{12}	126.98	203.20	39.48	113.15	254.28
Aq-E-2	7.002×10^3	48	154.96	8.652×10^{11}	123.56	179.00	40.52	101.73	215.14
Aq-F-2	4.946×10^3	48	152.72	8.282×10^{11}	167.45	169.08	31.15	96.78	204.53

Note. The leftmost column gives the simulation name, encoding the halo (A to F) and the resolution level (1 to 5; 1 is our highest resolution, 5 is the lowest). m_p is the particle mass in the high-resolution region, ϵ_G is the Plummer-equivalent gravitational softening length, r_{200} is the virial radius, defined as the radius enclosing a mean overdensity 200 times the critical value for closure, M_{200} is the mass within the virial radius, N_{200} is the total number of particles within r_{200}. Other characteristic properties of the haloes listed are the position (r_{max}) of the peak (V_{max}) of the circular velocity profile, as well as the one-dimensional velocity dispersion of the main halo (σ_{host}), and the peak (σ_{max}) of the velocity dispersion profile.

load balancing or numerical accuracy. Time-stepping is carried out with a kick-drift-kick leap-frog integrator where the time-steps are based on the local gravitational acceleration, together with a conservatively chosen maximum time-step for all particles. Pairwise particle interactions are softened with a spline of scalelength h_s, so that they are strictly Newtonian for particles separated by more than h_s. The resulting softening is roughly equivalent to a traditional Plummer-softening with scalelength $\epsilon_G \sim h_s/2.8$. The gravitational softening length is kept fixed in comoving coordinates throughout the evolution of all our haloes. The dynamics are then governed by a Hamiltonian and the phase-space density of the discretized particle system should be strictly conserved as a function of time (Springel 2005).

2.3 Halo selection

All haloes in the Aquarius suite were identified for resimulation in a 900^3-particle parent simulation of a $100\,h^{-1}$ Mpc box. The identification technique selects all $\sim 10^{12}$ M$_\odot$ haloes in the box and chooses, at random, a few of them that satisfy a mild isolation criterion (no neighbour exceeding half its mass within $1\,h^{-1}$ Mpc). This criterion is only imposed in order to remove haloes in the vicinity of massive groups and clusters, which may have evolved differently from the average.

Each halo is then resimulated at various resolutions, making sure that each resimulation shares the same power spectrum and phases at all resolved spatial frequencies. Initial displacements are imprinted using the Zeldovich approximation and a 'glass-like' uniform particle load (White 1996). The $100\,h^{-1}$ Mpc simulation box is divided into a 'high-resolution' region, which corresponds to the Lagrangian region surrounding the target halo, and a low-resolution region (the rest of the box), which is represented with a smaller number of particles with mass increasing with distance to the target halo. We have carefully designed the geometry of the high-resolution region in order to avoid contamination of the halo by massive low-resolution particles. Typically, about 30 per cent of particles in the high-resolution region end up in the virialized region of the final halo, and *no* higher mass particles end up within the virial radius of the final halo.

Table 1 lists some basic information about each simulation. This includes a symbolic simulation name, the particle mass in the high-

resolution region, m_p, the gravitational softening length, ϵ_G, the virial radius,[1] r_{200}, as well as the total mass, M_{200}, and the total number of particles, N_{200}, enclosed within r_{200}. Other structural parameters of interest include the location of the peak in the circular velocity profile, specified by r_{max} and V_{max}, as well as that of the velocity dispersion profile [σ_{max} and $r(\sigma_{max})$]. σ_{host} indicates the one-dimensional rms velocity of the main halo within r_{200} (excluding substructures).

Table 1 lists only information on the haloes used in this paper. A more complete list of numerical parameters may be found in Springel et al. (2008a). One of our haloes, labelled Aq-A, has been resimulated five times, spanning a factor of ~ 2000 in particle mass. Our naming convention uses the tags 'Aq-A' through 'Aq-F' to refer to each of the six Aquarius haloes. An additional suffix '1' to '5' denotes the resolution level. 'Aq-A-1' is our highest resolution calculation: it follows the surroundings of Aq-A with ~ 4.4 billion particles, ~ 1.1 billion of which end up within r_{200}. We have level-2 simulations of all six haloes, corresponding to between 100 and 200 million particles per halo (within r_{200}). The softening parameters of each simulation adopt the 'optimal' softening recommendation of P03, which aims to balance the number of time-steps required for accurate integration whilst minimizing the loss of spatial resolution.

2.4 Radial profiles

Our analysis uses spherically averaged profiles of the basic dynamical properties describing the structure of ΛCDM haloes: the density, circular velocity, velocity dispersion and anisotropy profiles. Typically, these are computed in 50 spherical shells equally spaced in

---

[1] We define the virial mass of a halo, M_{200}, as that contained within a sphere of mean density $200 \times \rho_{crit}$. The virial mass defines implicitly the virial radius, r_{200}, and virial velocity, $V_{200} = (GM_{200}/r_{200})^{1/2}$, of a halo, respectively. We note that other definitions of 'virial radius' have been used in the literature; the most popular of the alternatives adopts a density contrast (relative to critical) of $\Delta \approx 178\,\Omega_m^{0.45} \sim 100$ (for our adopted cosmological parameters, see Eke, Cole & Frenk 1996). We shall refer to these alternative choices, where appropriate, with a subscript indicating the value of Δ; i.e. r_{50} would be the virial radius obtained assuming $\Delta = 50$, and so an enclosed density 200 times the *mean* cosmic value.

$\log_{10} r$ (where r is the distance to the halo centre), and spanning the range $1.5 \times 10^{-4} < r/r_{200} < 3$. (When different choices for either the number of bins or the radial range are made, this is stated explicitly in the analysis below.) These concentric shells are centred at the location of the particle identified by the SUBFIND algorithm (Springel et al. 2001) as having the minimum gravitational potential. Extensive tests show that this procedure identifies the region where the local density of the main subsystem of each halo peaks, and is coincident in most cases (except perhaps major ongoing mergers between comparable-mass haloes) with the results of other methods, such as the 'shrinking sphere' method discussed by P03.

The mass density in each radial bin is estimated as the dark mass in the bin divided by its volume, and assigned to a radius corresponding to the bin centre. Circular velocities are computed by adding up the mass of each bin plus all interior ones, and assigned to the radius corresponding to the outer edge of the bin. The construction of velocity dispersion and anisotropy profiles is described in detail in Section 4.1. When differentiation is necessary, such as when computing the logarithmic slopes shown in Figs 5 and 6, we use a simple three-point Lagrangian interpolation to perform the numerical differentiation (as implemented by the DERIV subroutine of the IDL software package).

3 MASS PROFILES

3.1 Numerical convergence

We begin our study of the mass profile by using our series of resimulations of the Aq-A halo in order to assess the radial range where numerical convergence is achieved. Fig. 1 shows the mass profile of the five Aq-A resimulations; the left-hand panels show the spherically averaged density profile (multiplied by r^2 in order

to emphasize small departures) and the right-hand panels show the corresponding circular velocity profile. Lines of different colours correspond to different resimulations, as labelled. Arrows indicate $h_s = 2.8 \, \epsilon_G$, the length-scale where softened pairwise interactions become fully Newtonian.

This figure demonstrates the striking numerical convergence achieved in our resimulations. Outside some characteristic radius (which we discuss below), all the profiles are essentially indistinguishable from each other, even down to details such as 'bumps' in the outer regions caused by the presence of substructure. As discussed by Springel et al. (2008a), this reflects the high quality of the numerical integration of GADGET-3 and the careful approach we have taken for building our initial conditions; indeed, the Aq-A resimulations faithfully reproduce not only the properties of the main halo, but even the mass, location and internal structure of most major substructures.

Inevitably, near the centre the mass profiles diverge as a consequence of numerical limitations. Each profile is plotted down to the 'convergence radius' proposed by P03. These authors demonstrate that deviations from convergence depend (for appropriate choices of other numerical parameters) solely on the number of particles, and scale roughly with the collisional 'relaxation' time, t_{relax}. Expressed in units of the circular orbit time-scale at r_{200} (which is of the order of the age of the Universe), $\kappa = t_{\text{relax}}/t_{\text{circ}}(r_{200})$, the relaxation time may be written as

$$\kappa(r) = \frac{N}{8 \ln N} \frac{r/V_c}{r_{200}/V_{200}} = \frac{\sqrt{200}}{8} \frac{N(r)}{\ln N(r)} \left[\frac{\overline{\rho}(r)}{\rho_{\text{crit}}} \right]^{-1/2}, \quad (1)$$

where $N = N(r)$ is the enclosed number of particles and $\overline{\rho}(r)$ is the mean enclosed density within r.

According to P03, deviations of roughly 10 per cent are expected in the V_c profile where $\kappa \approx 1$, and they adopted this condition to define the convergence radius, r_{conv}. Stricter convergence demands
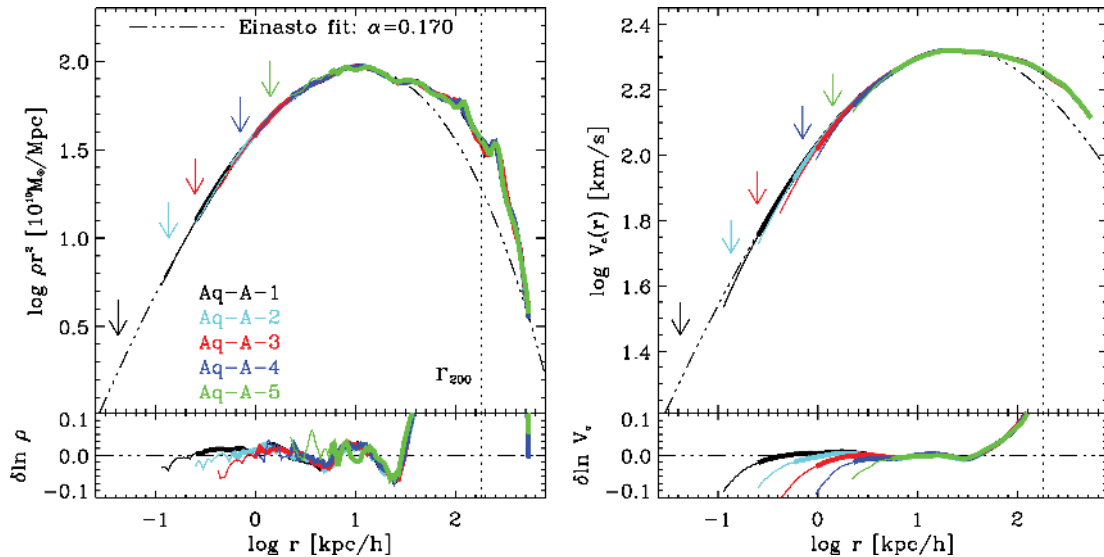
Figure 1. Spherically averaged density (left-hand panel) and circular velocity (right-hand panel) profiles for the Aq-A halo simulation series. Different colours correspond to different resolution runs, as labelled in the figure. The density profile is multiplied by r^2 in order to emphasize small deviations. The bumps in the outer regions may be traced to the presence of substructure and unrelaxed tidal debris. Profiles are shown from $\sim 3r_{200}$ down to the 'convergence radius', $r_{\text{conv}}^{(1)}$, corresponding to the radius where the relaxation time, t_{relax}, is of the order of the age of the Universe. The thick portion of each profile indicates the region $r > r_{\text{conv}}^{(7)}$ where t_{relax} is more than seven times the age of the universe and where stricter convergence is achieved. Outside $r_{\text{conv}}^{(7)}$ circular velocity estimates converge to better than 2.5 per cent (see Fig. 2). The dot–dashed line shows an Einasto profile with $\alpha = 0.17$ matched at (r_{-2}, ρ_{-2}), the peak in the $r^2 \rho$ profile. This provides an excellent fit to the structure of the inner regions of the halo, as shown by the residuals plotted in the bottom panels. Arrows indicate the softening length h_s of each simulation.

larger values of κ, and we shall use a superscript on $r_{\rm conv}$ to denote the value of κ adopted for its definition. For instance, $r_{\rm conv}^{(1)} = r_{\rm conv}^{(\kappa=1)}$ corresponds to $\kappa = 1$.

Profiles in Fig. 1 are thus plotted in the range $[r_{\rm conv}^{(1)}, 3\,r_{200}]$. As shown in the bottom-right panel, this inner radius indeed corresponds to the point where systematic deviations in $V_{\rm c}(r)$ reach $\sim$10 per cent. It is also clear from this figure that convergence in the local density profile is always much easier to achieve, so concentrating our analysis on the enclosed mass profile, or on the circular velocity, is a conservative approach.

Although each halo converges over a different radial range, the departures from convergence are all similar when expressed in terms of κ. This is shown in the top panel in Fig. 2, where differences in $V_{\rm c}$ from our highest resolution halo, Aq-A-1, are shown as a function of κ for the other Aq-A resimulations. Deviations of $\sim$10 per cent are typical at $\kappa = 1$; convergence to better than $\sim$2.5 per cent, on the other hand, requires $\kappa \approx 7$ (indicated by the right dashed vertical line).

We may use these results to estimate convergence radii for our highest resolution run, Aq-A-1: its $V_{\rm c}$ profile converges to better than 10 per cent for radii $r > r_{\rm conv}^{(1)} = 112\,h^{-1}$ pc; 2.5 per cent convergence or better is expected for $r > r_{\rm conv}^{(7)} = 253\,h^{-1}$ pc (see bottom panel of Fig. 2). Convergence radii for various values of κ are listed in Table 2 for each simulated halo.

3.2 Fitting formulae

The fitting formulae we have used to describe the mass profile of our simulated haloes are the following: (i) The NFW profile, given by

$$\rho(r) = \frac{\rho_{\rm s}}{(r/r_{\rm s})(1 + r/r_{\rm s})^2}; \tag{2}$$

(ii) the modification to the NFW profile proposed by M99,

$$\rho(r) = \frac{\rho_{\rm M}}{(r/r_{\rm M})^{1.5}[1 + (r/r_{\rm M})^{1.5}]}, \tag{3}$$

and (iii) the Einasto profile,

$$\ln[\rho(r)/\rho_{-2}] = (-2/\alpha)[(r/r_{-2})^\alpha - 1]. \tag{4}$$

Because each of these formulae defines the characteristic parameters in a slightly different way, we choose to reparametrize them in terms of r_{-2} and $\rho_{-2} \equiv \rho(r_{-2})$, which identify the 'peak' of the $r^2\rho$ profile shown in the left-hand panels of Fig. 1. This marks the radius where the logarithmic slope of the profile, $\gamma(r) = -\mathrm{d}\ln\rho/\mathrm{d}\ln r$, equals the isothermal value, $\gamma = 2$.

The characteristic radius, r_{-2}, is a well-defined scalelength which is relatively easy to identify in each halo without resorting to any particular fitting formula. In practice, we determine r_{-2} by computing the logarithmic slope profile, $\gamma(r)$, and identifying where a low-order polynomial fit to it intersects the isothermal value. Each $r^2\rho$ profile is then visually inspected in order to ensure that r_{-2} corresponds to the main peak of the profile, and that it is not unduly influenced by secondary peaks that arise as the result of substructure. (See the left-hand panels of Fig. 1.) Table 2 lists r_{-2} and ρ_{-2} for all our simulated haloes. Note that for the NFW profile, $r_{-2} = r_{\rm s}$ and $\rho_{-2} = \rho_{\rm s}/4$, while for the Moore profile, $\rho_{-2} = (4/3)\,\rho_{\rm M}$ and $r_{-2} = 2^{-2/3}\,r_{\rm M}$.

We note that, unlike NFW or M99, when α is allowed to freely vary the Einasto profile is a three-parameter fitting formula. This is not, of course, the only possible extension of NFW-like profiles
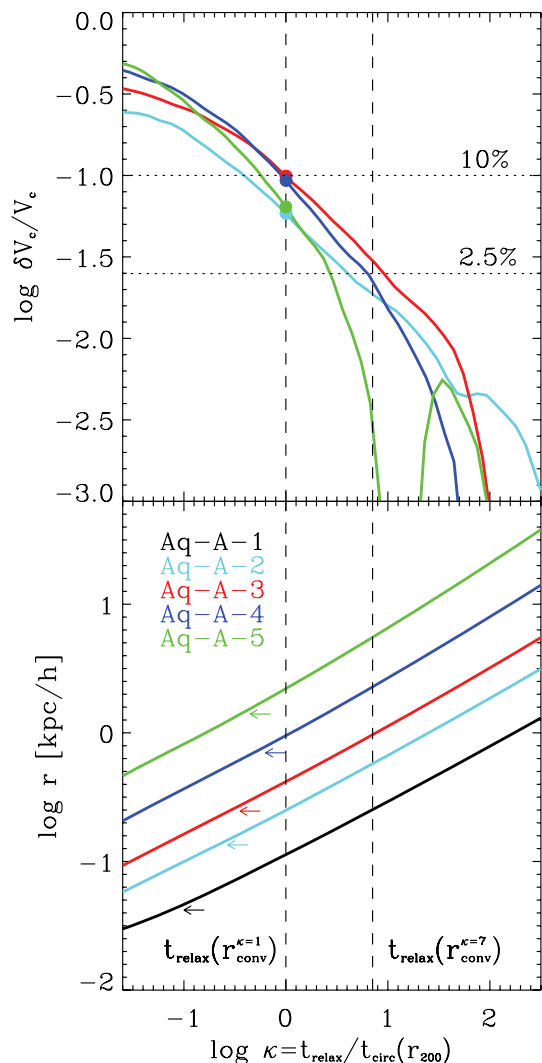
Figure 2. Top panel: fractional deviations in the circular velocity profile of the Aq-A convergence series versus the (enclosed) relaxation time, $t_{\rm relax}$, expressed in units of the circular orbit period at the virial radius, $t_{\rm circ}(r_{200})$. Deviations are measured relative to the highest resolution halo, Aq-A-1. Note that departures from convergence for all simulations are similar when expressed this way, indicating that $t_{\rm relax}$ is the main parameter determining convergence. Solid circles mark the location of the convergence criterion proposed by P03. Note that $V_{\rm c}$ estimates converge there to about 10 per cent. A stricter convergence criterion, for example 2.5 per cent convergence in $V_{\rm c}$, is achieved at larger radii, where $t_{\rm relax} \sim 7\,t_{\rm circ}(r_{200})$ (right vertical line). Bottom panel: relaxation time versus radius for all five Aq-A simulations. Arrows indicate $h_{\rm s} = 2.8\,\epsilon_{\rm G}$, the length-scale where pairwise interactions become Newtonian.

which allows for a variable shape with the aid of an extra free parameter. For example, Merritt et al. (2006) compared N-body haloes with the three-parameter Einasto formula, as well as with the anisotropic model of Dehnen & McLaughlin (2005) and with the deprojected Sersic (1968) model of Prugniel & Simien (1997). Merritt et al. conclude that, overall, Einasto's formula performs best. Therefore, we adopt it here for the rest of our analysis, although we do not exclude the possibility that other three-parameter formulae may perform at least as well as Einasto's. A full exploration of this issue is beyond the scope of this paper.

Table 2. Fit parameters of Aquarius haloes.

Halo	$r_{\mathrm{conv}}^{(1)}$ (kpc h^{-1})	$r_{\mathrm{conv}}^{(7)}$ (kpc h^{-1})	ρ_{-2} ($10^{10}\,h^2\,\mathrm{M}_\odot\,\mathrm{Mpc}^{-3}$)	r_{-2} (kpc h^{-1})	α	χ	χ_{r}	γ_{max}
Aq-A-1	0.113	0.253	7.462×10^5	11.05	0.170 ± 0.0259	-1.898	-1.948	0.894
Aq-A-2	0.250	0.575	7.322×10^5	11.15	0.163 ± 0.0249	-1.917	-1.976	1.051
Aq-A-3	0.417	0.966	7.456×10^5	11.09	0.174 ± 0.0266	-1.926	-1.995	1.128
Aq-A-4	0.952	2.277	6.501×10^5	11.90	0.160 ± 0.0248	-1.991	-2.061	1.321
Aq-A-5	2.206	5.530	7.534×10^5	11.02	0.165 ± 0.0268	-2.015	-2.111	1.493
Aq-B-2	0.219	0.507	1.830×10^5	16.79	0.173 ± 0.0123	-1.868	-1.938	1.039
Aq-C-2	0.248	0.573	4.973×10^5	14.37	0.159 ± 0.0125	-1.948	-2.010	1.077
Aq-D-2	0.281	0.652	2.075×10^5	20.30	0.170 ± 0.0124	-1.862	-1.942	1.070
Aq-E-2	0.223	0.516	2.058×10^5	17.88	0.130 ± 0.0200	-1.912	-1.947	1.084
Aq-F-2	0.209	0.486	1.673×10^5	18.84	0.145 ± 0.0167	-1.911	-1.980	1.298

Note. The first column labels each halo, as in Table 1, the second and third list the convergence radii obtained for $\kappa = 1$ and 7. These radii, $r_{\mathrm{conv}}^{(1)}$ and $r_{\mathrm{conv}}^{(7)}$, respectively, correspond to where departures from convergence in the circular velocity are expected to be of the order of 10 and 2.5 per cent. The characteristic scale radius r_{-2} corresponds to where the logarithmic slope equals the isothermal value; $\rho_{-2} = \rho(r_{-2})$, and α is the best-fitting Einasto parameter. The uncertainty in α indicates the range where $\Delta Q/Q$ deviates by less than 50 per cent from the absolute minimum shown in Fig. 4. Strictly, these are non-symmetric, so we conservatively quote the largest deviation, positive or negative. χ refers to the exponent of the best-fitting power-law describing the ρ/σ^3 profile. χ_{r} is analogous to χ, but for $\rho/\sigma_{\mathrm{r}}^3$, where σ_{r} is the rms velocity in radial motions. χ and χ_{r} are computed by minimizing residuals in the region $r_{\mathrm{conv}}^{(1)} < r < r_{-2}$. Finally, γ_{max} lists the value of the maximum asymptotic slope of the density profile cusp, measured at $r = r_{\mathrm{conv}}^{(7)}$.

3.3 Fitting procedure

Best-fitting parameters are found by minimizing the deviation between model and simulation across all bins in a specified radial range. In the case of the density profile, the best fit is found by minimizing the figure-of-merit function, Q^2, defined by

$$Q^2 = \frac{1}{N_{\mathrm{bins}}} \sum_{i=1}^{N_{\mathrm{bins}}} \left(\ln \rho_i - \ln \rho_i^{\mathrm{model}} \right)^2. \qquad (5)$$

This function provides an intuitively simple measure of the level of disagreement between simulated and model profiles. It is dimensionless; it weights different radii logarithmically and, for given radial range, Q^2 is approximately independent of the number of bins used in the profile. Thus, minimizing Q^2 yields for each halo well-defined estimates of a model's best-fitting parameters. Note that when Q is small, it is just the rms fractional deviation of the data from the model.

It is less clear how to define a goodness-of-fit measure associated with Q^2 and, consequently, how to assign statistically meaningful confidence intervals to the best-fitting parameter values. This difficulty arises because, at very high resolution of the simulations analysed here, discreteness noise in the binned density estimates is negligible. The figure of merit of a fit therefore depends not only on how faithfully a model approximates a halo but also on the presence of individual halo features that no simple fitting formula can hope to reproduce. These distinct features are present on small scales (substructure) and large scales (such as streams, asphericity and other relics of each halo's specific assembly history; see e.g. Vogelsberger et al. 2009). As a result, bin-to-bin residuals are distinctly non-Gaussian and highly correlated, precluding the use of simple statistical tools such as the χ^2 distribution in order to assess goodness of fit.

Assessing the acceptability of various Q values would require the definition of a detailed statistical model in order to reliably measure the departures of individual haloes from a smooth profile whose average shape (and scatter) could be obtained directly by averaging various numerical realizations of haloes of the same mass.

Unfortunately, such procedure is unlikely to be robust with only six haloes in our sample.

Therefore, we limit our analysis to comparing the minimum-Q values obtained with various formulae, and to discussing how Q changes as the fitting parameters are varied. The actual value of Q is, after all, a reliable and objective measure of the average per-bin deviation from a particular model. As we discuss below, this is, in many cases, enough to prefer unequivocally one fitting formula over another and to make a compelling case for the need of an extra parameter in the fit.

3.4 Einasto versus NFW versus M99

The left-hand panel of Fig. 3 compares the density profiles of all six level-2 Aquarius haloes, after scaling radii to r_{-2} and densities to ρ_{-2}. The right-hand panel shows the circular velocity profiles, scaled in an analogous manner to match the peak of the profile, identified by r_{max} and V_{max}. In these scaled units, the fitting formulae introduced in Section 3.2 are curves of fixed shape and normalization, as shown by the thin solid, dashed and dot–dashed curves in Fig. 3. (The Einasto curve adopts $\alpha = 0.159$ in this figure.)

Comparison with the simulations (thick curves) indicates that there is a clear mismatch between the shape of the halo profiles and those of the NFW and M99 fitting formulae. This is not just a result of enforcing the r_{-2}–ρ_{-2} scaling. We illustrate this by showing, in the two bottom panels of Fig. 3, residuals from *best fits* obtained by adjusting *both* fit parameters of the NFW and M99 profiles (r_{-2} and ρ_{-2}) in order to minimize Q^2. (The radial range chosen for these fits is $r_{\mathrm{conv}}^{(1)} < r < 0.5\,r_{200}$.) Note the 'S' shape in the residuals, which are largest (and increasing) at the innermost radius of the profile. Because of the shape mismatch, extrapolating either the NFW or M99 fits further inwards, to regions less well resolved numerically, is almost guaranteed to incur substantial error.

The large-scale radial trend of the residuals from the best Einasto fits (middle panels of Fig. 3), on the other hand, is rather weak, suggesting that the shape of the simulated halo profiles is much better accommodated by this formula. This is *not* just a result of the extra shape parameter in the Einasto formula: even when keeping
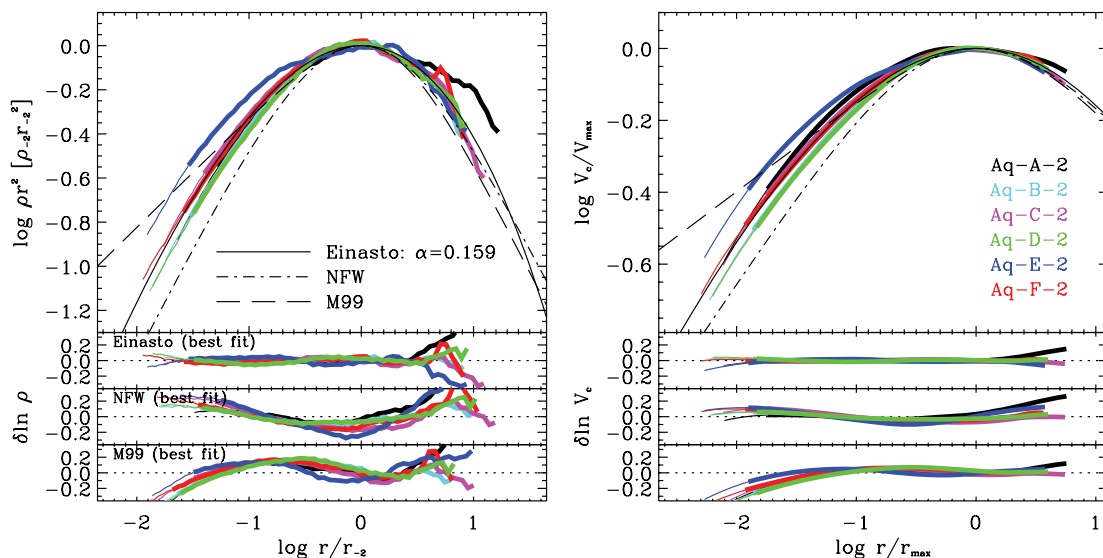
Figure 3. Left-hand panel: spherically averaged density profiles of all level-2 Aquarius haloes. Density estimates have been multiplied by r^2 in order to emphasize details in the comparison. Radii have been scaled to r_{-2}, the radius where the logarithmic slope has the 'isothermal' value, -2. Thick lines show the profiles from $r_{conv}^{(7)}$ outwards; thin lines extend inwards to $r_{conv}^{(1)}$. For comparison, we also show the NFW and M99 profiles, which are fixed in these scaled units. This scaling makes clear that the inner profiles curve inwards more gradually than NFW, and are substantially shallower than predicted by M99. The bottom panels show residuals from the *best fits* (i.e. with the radial scaling free) to the profiles using various fitting formulae (Section 3.2). Note that the Einasto formula fits all profiles well, especially in the inner regions. The shape parameter, α, varies significantly from halo to halo, indicating that the profiles are not strictly self-similar: no simple physical rescaling can match one halo on to another. The NFW formula is also able to reproduce the inner profiles quite well, although the slight mismatch in profile shapes leads to deviations that increase inwards and are maximal at the innermost resolved point. The steeply cusped Moore profile gives the poorest fits. Right-hand panel: same as the left, but for the circular velocity profiles, scaled to match the peak of each profile. This cumulative measure removes the bumps and wiggles induced by substructures and confirms the lack of self-similarity apparent in the left-hand panel.

α fixed to a single value, residuals are smaller and have less radial structure than those from either NFW or M99.

We show this in Fig. 4, where we plot the minimum-Q (Q_{min}) values of the best Einasto fits for all six level-2 Aquarius haloes, as a function of the shape parameter α. For given value of α, the remaining two free parameters of the Einasto formula are allowed to vary in order to minimize Q^2. Different line types correspond to different numbers of bins used to construct the profile (from 20 to 50), chosen to span in all cases the same radial range, $0.01 < r/r_{-2} < 5$, a factor of 500 in radius. Minimum-Q values are computed using a similar procedure for the NFW and M99 formulae, and are shown, for each halo, with symbols of corresponding colour.

In terms of Q_{min}, Einasto fits are consistently superior to NFW or M99, whether or not the α parameter is adjusted freely. For example, for *fixed* $\alpha = 0.15$, *all* Einasto best fits have minimum-Q values below ~ 0.03. For comparison, best NFW and M99 fits have an average $\langle Q_{min} \rangle \sim 0.06$ and 0.095, respectively. These numbers correspond to $N_{bins} = 20$, but they are rather insensitive to N_{bins}, as may be judged from the small difference between the various lines corresponding to each halo in Fig. 4.

We emphasize that, although the improvement obtained with Einasto's formula is significant, NFW fits are still excellent, with a typical rms deviation of just ~ 6 per cent over a range of 500 in radius. The use of the NFW formula may thus be justified for applications where this level of accuracy is sufficient over this radial range.

When α is adjusted as a free parameter, $\langle Q_{min} \rangle \sim 0.018$ for Einasto fits. Furthermore, there is, for each halo, a well-defined value of α that yields an absolute minimum in Q. The Q-dependence on α about this minimum is roughly symmetric and, as expected, nearly independent of the number of bins used in the profile. The
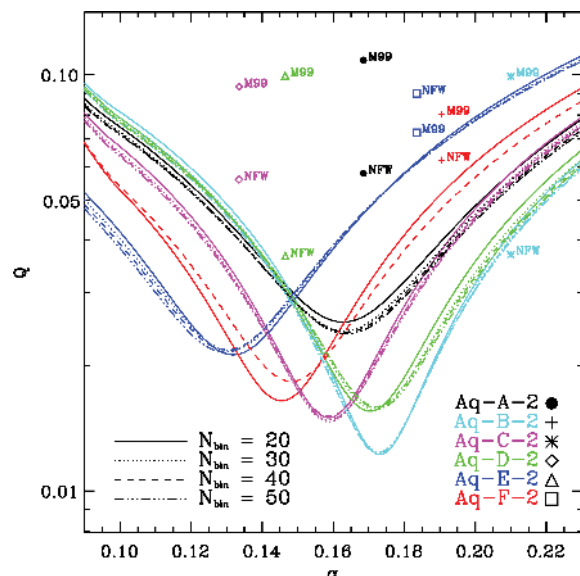
Figure 4. Minimum-Q values as a function of the Einasto parameter α for best fits to all level-2 halo profiles in the radial range $0.01 < r/r_{-2} < 5$. Colours identify different haloes, and line types identify the number of bins chosen for the profile. The minimum-Q values obtained for NFW and M99 best fits are also shown, and are plotted at arbitrary values of α for clarity. Note that Einasto fits are consistently better than NFW which are consistently better than M99, and that a significant improvement in Q is obtained when letting α vary in the Einasto formula. Q is approximately independent of the number of bins used in the profile, and is minimized for different values of α for each individual halo (see the text for further details).

minimum in Q is sharp; a shift of just 0.015 in α typically leads to an increase of ~50 per cent in Q around the minimum. Given that the value of α that minimizes Q varies from 0.130 for Aq-E-2 to 0.173 for Aq-B-2, we conclude that the improvement obtained when allowing α to vary is significant. We quote nominal 'error bars' for α in Table 2 that bracket the interval where Q deviates by less than 50 per cent from the absolute minimum in Fig. 4.

3.5 Self-similarity?

The need for a variable α discussed above illustrates one of our main findings: namely that the mass profiles of our Aquarius haloes *are not strictly self-similar*. The shapes of the profiles are subtly but significantly different from each other, and no rescaling can match one exactly to another. Halo Aq-E-2 provides the most striking example, deviating from halo Aq-D-2, for example, by almost a factor of 2 in density at $\sim0.03\,r_{-2}$. The same differences in mass profile shape are also easily appreciated in the scaled circular velocity profiles, which indicate that the departures from similarity are genuine and not just caused by inaccuracies in the scaling or by the 'bumps and wiggles' caused by unrelaxed tidal debris and substructure.

We have verified this further by performing the same analysis after removing bound substructure clumps identified by SUBFIND: the same conclusion applies to the 'cleaned' profiles of the main smooth halo. With hindsight, this is perhaps not too surprising. Bound substructures do not amount to more than ~10 per cent of the halo mass (Springel et al. 2008a), and therefore cannot alter the results discussed above.

We have also checked that the differences in α are not caused by transient departures from equilibrium or numerical resolution: the same qualitative trends, and indeed very similar α values, are seen at earlier times and in runs with fewer particles. There also seems to be little correlation between α and the overall triaxiality of the system; however, we shall only deal here with spherically averaged profiles, and defer a detailed study of departures from sphericity to a later paper.

Although the departures from similarity appear significant, we must also emphasize that they are rather subtle and are only clearly evident because of the large radial range resolved by our simulations, about *three decades* in radius within the virialized region of a halo. Simulations with more limited numerical resolution have hinted at this but had difficulty making such a compelling case for non-similarity (see e.g. Navarro et al. 2004; Merritt et al. 2005, 2006; Stoehr 2006).

3.6 The cusp

It is clear from the residuals in the bottom panels of Fig. 3 that, near the centre, the M99 profile approximates the simulated haloes more poorly than either NFW or Einasto. The weak performance of the M99 formula may be traced to its steep asymptotic inner slope, $\rho \propto r^{-1.5}$. Indeed, all six Aquarius haloes have *measured* slopes in the inner regions that are substantially shallower than -1.5. This is shown in Figs 5 and 6, where the thick portion of each curve corresponds to $r > r_{conv}^{(7)}$ and the innermost point plotted to $r_{conv}^{(1)}$. In all cases, the logarithmic slopes converge well inside $r_{conv}^{(7)}$, and only minor deviations may be seen at radii beyond $r_{conv}^{(1)}$.

Interestingly, the slope of the Aq-A-1 profile at $r = r_{conv}^{(7)}$ is exactly -1 and becomes shallower inwards, so it is clear that at least for this halo we are able to resolve a region where the dark matter profile has become shallower than -1, the asymptotic value of the NFW profile. Fig. 6 shows the radial dependence of the logarithmic slope
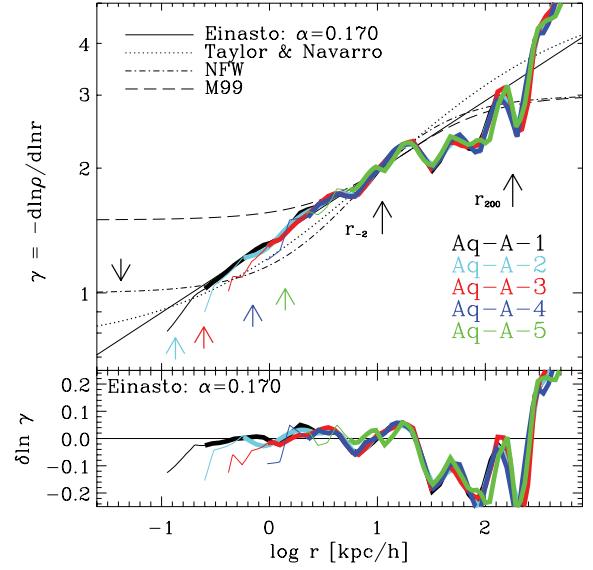

Figure 5. Logarithmic slope of the density profile as a function of radius for our Aq-A convergence series. As in other plots, thick lines show results for $r > r_{conv}^{(7)}$, thin lines extend the profiles down to the less strict convergence radius $r_{conv}^{(1)}$. Comparison shows that excellent numerical convergence for the slope is achieved down to a radius intermediate between these two convergence radii. Applied to the highest resolution Aq-A-1 simulation, this implies that the slope is shallower than the asymptotic value of the NFW profile (r^{-1}) in the inner regions. We see no sign of convergence to an asymptotic inner power law. Instead, the profiles get shallower towards the centre as predicted by the Einasto formula (a straight line in this plot). The 'critical solution' of Taylor & Navarro (2001) (which has an $r^{-0.75}$ asymptotic inner cusp) does better than NFW but not as well as Einasto in reproducing the inner profile of the halo.
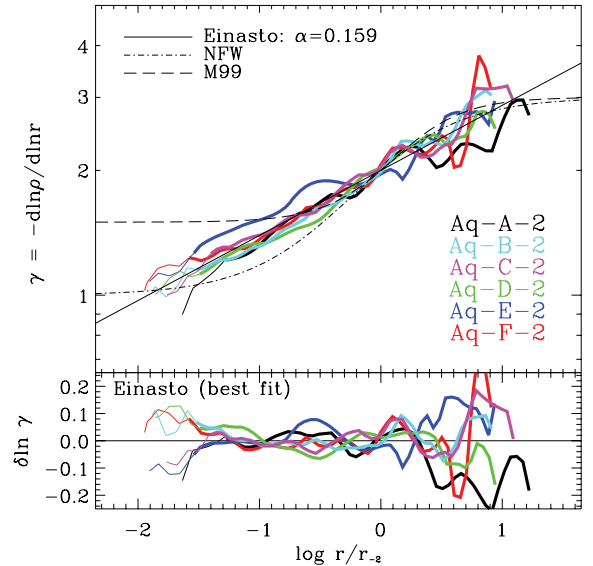
Figure 6. As Fig. 5, but for all level-2 resolution Aquarius haloes, after scaling radii to r_{-2}.

for all six level-2 haloes and confirms the general applicability of the Aq-A results: the *measured* slopes of all haloes approach -1 (and are certainly shallower than -1.5) at the innermost resolved point.

Figs 5 and 6 also make clear that there is no sign that the profiles are approaching power-law behaviour near the centre: they keep
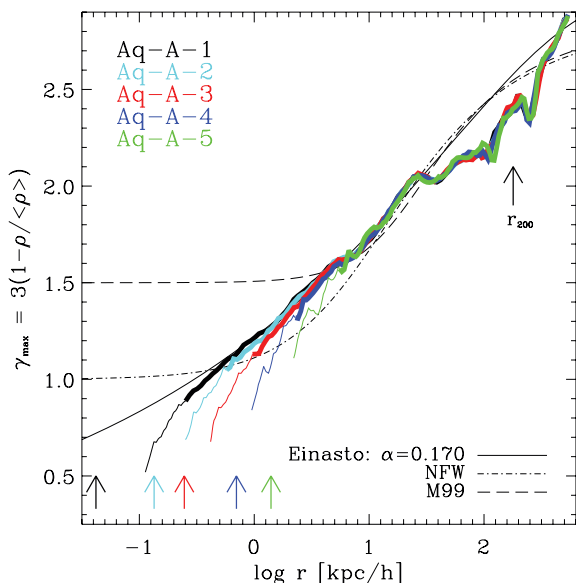
Figure 7. Maximum value of the asymptotic inner slope of the density cusp, as a function of radius for our Aq-A convergence series. Excellent numerical convergence is achieved at radii comparable to $r_{conv}^{(7)}$ [the inner limit of the thick lines; thin lines extend down to $r_{conv}^{(1)}$]. This shows that there is not enough mass near the centre of Aq-A to sustain a cusp steeper than $\rho \propto r^{-0.9\pm0.1}$. Arrows are as in Fig. 1.

Figure 8. As Fig. 7, but for our six level-2 Aquarius haloes. Results are similar in all cases and rule out cusps steeper than r^{-1} for ΛCDM haloes.

getting shallower to the innermost resolved radius. This behaviour is well captured by the Einasto model, where the logarithmic slope is simply a power law of radius, $d \ln \rho / d \ln r \propto r^\alpha$. Our results thus rule out recent claims of cusps as steep as $r^{-1.2}$ in typical ΛCDM haloes (Diemand et al. 2004, 2005, 2008).

This conclusion is unlikely to depend on the details of our profile construction and/or fitting procedures. Indeed, as we show in the next section, there is actually *not enough mass* within the innermost resolved radius to allow for a cusp as steep as $r^{-1.2}$. Recent work by Stadel et al. (2009), also based on very high-resolution simulations, agrees with our present conclusions, and argues for asymptotic inner slopes shallower than -1, as previously suggested by Navarro et al. (2004).

3.7 The asymptotic inner slope

The results presented above do not preclude the possibility that a shallow power-law cusp may be present in the innermost regions which are still unresolved in our simulations. It is therefore interesting to estimate the *maximum* value that the slope of such a cusp may take. This is constrained, at any radius, by the total enclosed mass and the local value of the spherically averaged density: slopes steeper than γ_{max} require more mass than is available within that radius. This constraint assumes only that the logarithmic slope is monotonic with radius and that the halo is not hollow. It is then straightforward to show that the maximum possible inner asymptotic slope is $\gamma_{max} = 3[1 - \rho(r)/\bar{\rho}(r)]$, where $\bar{\rho}(r)$ is the mean density enclosed within r. Evaluated at the innermost radius where both local density and enclosed mass (or, equivalently, circular velocity) have converged, this quantity provides an important constraint on the density profile at radii that remain unresolved even in our best simulations.

We show this parameter as a function of radius for our Aq-A convergence series in Fig. 7. This figure shows that γ_{max} converges to better than 0.1 for $r > r_{conv}^{(7)}$ (the innermost point of the thick
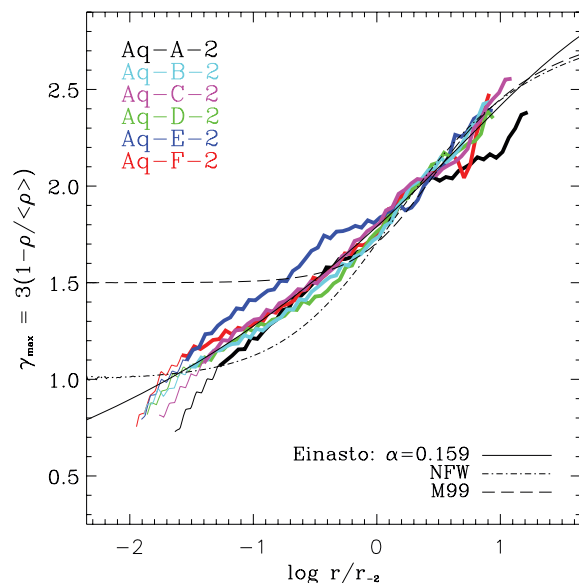
portion of the profiles). Our data for Aq-A thus indicate that there is not enough mass in the unresolved region to support a cusp steeper than $r^{-0.9\pm0.1}$. Fig. 8 shows that the results for Aq-A are not exceptional: all our level-2 Aquarius haloes suggest maximum possible asymptotic slopes of about -1.

3.8 Halo centring

Although the statistical uncertainties in the binned density estimates are extremely small due to the large numbers of particles in our simulations, there is one potential source of systematic error that may bias the results: the choice of halo centre. Missing the proper halo centre, where the dark matter density peaks, would lead to artificially shallow profiles and to depressed central density estimates. We explore this in Fig. 9, where we show, for the case of Aq-A-2, the density and logarithmic slope profiles that result from choosing as halo centre positions shifted by 1, 2, 4, 8 and 16 gravitational softening scalelengths from the location of the particle with minimum potential energy (our fiducial choice). These panels explicitly demonstrate the expected effect. They also show that our fiducial choice maximizes the density estimates near the centre as well as the steepness of the logarithmic slope. Our conclusion that cusps as steep as $\gamma = -1.2$ are inconsistent with our results is thus unaffected by our choice of halo centre.

4 DYNAMICAL PROFILES

4.1 Velocity dispersion structure

Fig. 10 shows velocity dispersion and anisotropy profiles for our Aq-A series and demonstrates that the excellent numerical convergence of our simulations extends to their velocity dispersion structure. The velocity dispersion (squared) is computed simply as twice the specific kinetic energy in each spherical shell and the anisotropy as $\beta = 1 - \sigma_t^2/(2\sigma_r^2)$, where σ_t^2 and σ_r^2 are the (squared) velocity dispersion in tangential and radial motions, respectively. Besides numerical convergence, the panels in this figure illustrate two
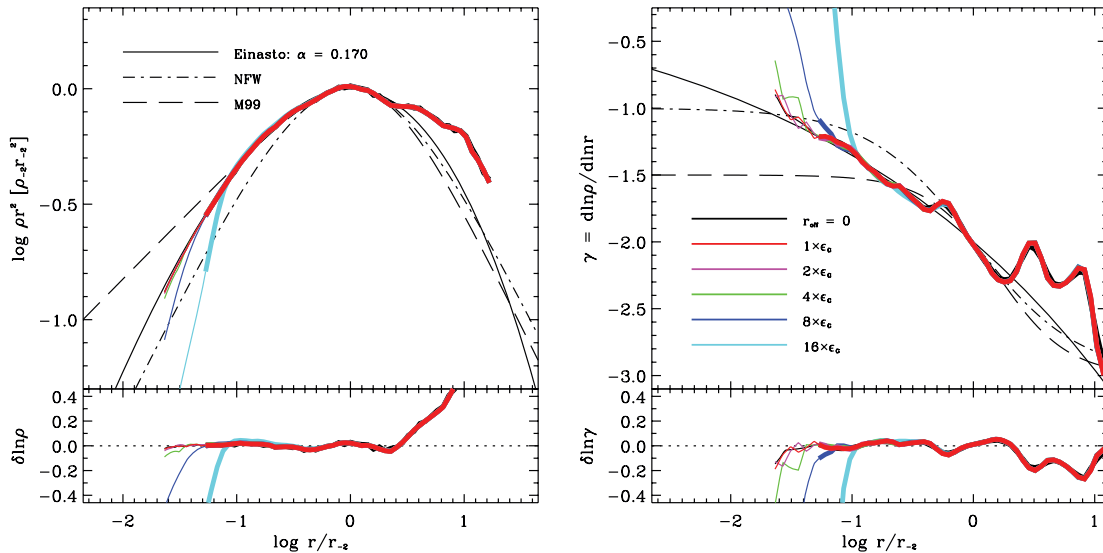
Figure 9. Density (left-hand panel) and logarithmic slope (right-hand panel) profiles for halo Aq-A-2. Each curve corresponds to the profiles obtained after choosing as halo centre a position shifted by various multiples of the gravitational softening scalelength from the position of the particle with minimum potential energy (our fiducial choice). These panels clearly demonstrate that our fiducial choice maximizes the density estimates near the centre and results in the steepest logarithmic slopes. Bottom panels show residuals from the best Einasto fit shown in the upper panels.
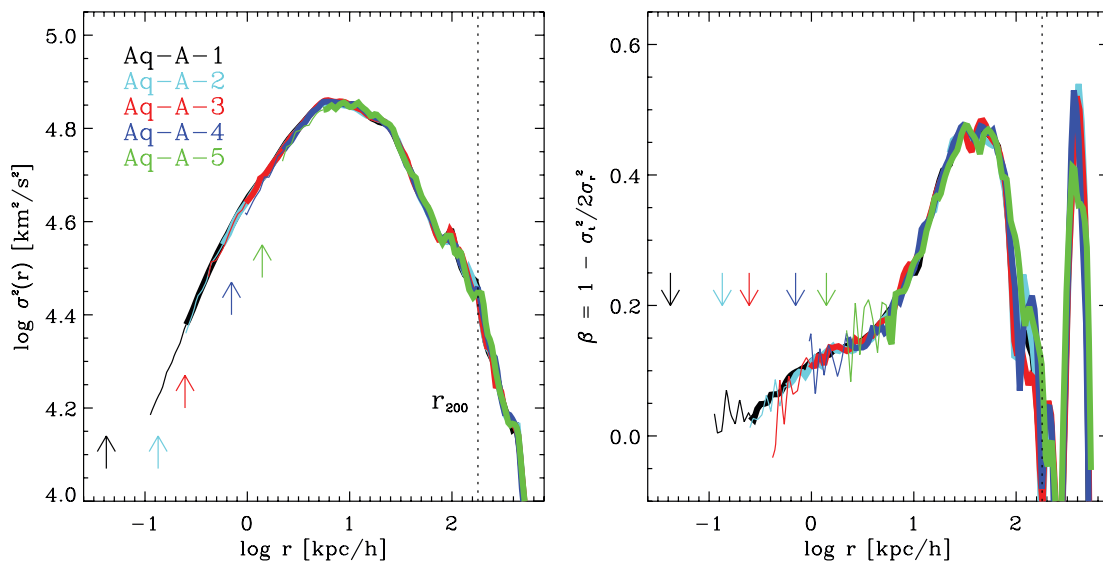

Figure 10. Left-hand panel: velocity dispersion profiles for our Aq-A convergence series. Arrows, line types and colours are as in Fig. 1. Note the excellent numerical convergence. The shape of the velocity dispersion profile is remarkably similar to that of the $r^2\rho$ profile shown in Fig. 1, highlighting the intimate connection between the density and velocity dispersion profiles which is responsible for the power-law behaviour of the pseudo-phase-space density profile discussed in Section 4.4. Right-hand panel: anisotropy profiles for the Aq-A convergence series. Note the non-monotonic variation with radius: the halo is nearly isotropic near the centre, is dominated by radial motions at intermediate radii, but becomes markedly less anisotropic near the virial radius.

important points. The first concerns the shape of the velocity dispersion profiles (left-hand panel in Fig. 10), which is remarkably similar to that of the $r^2\rho$ profiles shown in Fig. 1. This coincidence suggests an intimate connection between density and velocity dispersion, which we explore in more detail in Section 4.4. The second point concerns the anisotropy profile, which is clearly non-monotonic. It is nearly isotropic at the centre, becomes radially anisotropic at intermediate radii, but the dominance of radial motions decreases again near the virial radius. As shown in Fig. 11, these properties appear to be rather general, since all six Aquarius haloes have non-monotonic anisotropy profiles and similar velocity dispersion profile shapes.

4.2 Self-similarity?

Fig. 11 also demonstrates a clear lack of self-similarity in the structure of the simulated haloes. We have chosen to emphasize this by rescaling all profiles so as to match the peak of the $\sigma(r)$ curve, which occurs at $r(\sigma_{\max})$. This scaling demonstrates that, as with the density profiles, the *shape* of the $\sigma(r)$ profiles differs subtly but significantly amongst haloes. We have checked that these differences in shape are not due to bound subhaloes; removing all the subhaloes identified by our SUBFIND algorithm and recalculating the dispersion and anisotropy profiles results in only rather minor changes. The most striking case is again that of halo Aq-E-2 (blue curve), whose
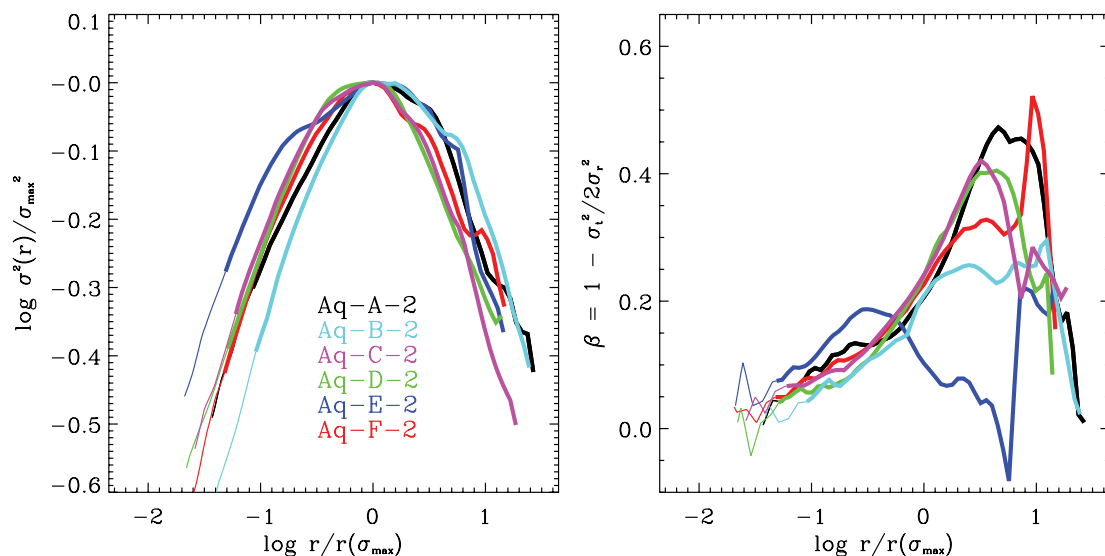
Figure 11. As Fig. 10, but for all six level-2 resolution Aquarius haloes, scaled to match at the peak of the profile, identified by σ_{max} and $r(\sigma_{max})$. This scaling highlights small but significant departures from similarity in the velocity dispersion structure of ΛCDM haloes. Note the correspondence in shape between the velocity dispersion and $r^2\rho$ profiles shown in Fig. 1, which reflects the 'universal' pseudo-phase-space density profile of the haloes (Fig. 14). Also note that the non-monotonic behaviour of the anisotropy highlighted in Fig. 10 is common to all six haloes.

$\sigma(r)$ profile is much broader than the others. Recall that this halo also stands out in Fig. 3 as having an unusually broad $r^2\rho$ profile. Halo Aq-E-2 also has an unusual velocity anisotropy profile, with less predominance of radial motions than the rest of the series. The departures from similarity in mass and velocity structure therefore seem closely linked, suggesting that these haloes may share a common property that combines density and velocity dispersion. We explore this in Section 4.4.
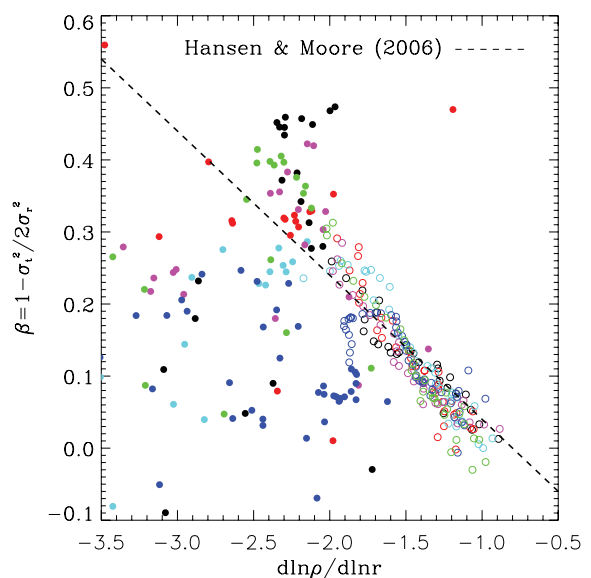
4.3 Anisotropy–slope relation

We may use the results of the previous section to assess recent claims by Hansen & Moore (2006) of a general connection between the local values of logarithmic slope, γ, and the velocity anisotropy, β. We show this in Fig. 12, where we plot β versus γ for all level-2 Aquarius haloes. Open circles correspond to the inner regions of the halo [$r_{conv}^{(1)} < r < r_{-2}$], whereas filled circles correspond to the outer regions ($r_{-2} < r < r_{200}$). As in other figures, different colours correspond to the different Aquarius haloes. The relation proposed by Hansen & Moore is shown by a dashed line and accounts reasonably well (albeit not perfectly) for our data in the inner regions where both the anisotropy and the logarithmic slope are monotonic functions of r.

However, there are large departures from this relation in the outer regions, where the density profile steepens further but the velocity ellipsoid tends to become less anisotropic. The failure of the Hansen & Moore relation in the outer regions is not unexpected since γ, unlike β, is monotonic with radius. We conclude that if a simple relation links anisotropy and slope, it can only hold in the inner regions of haloes.
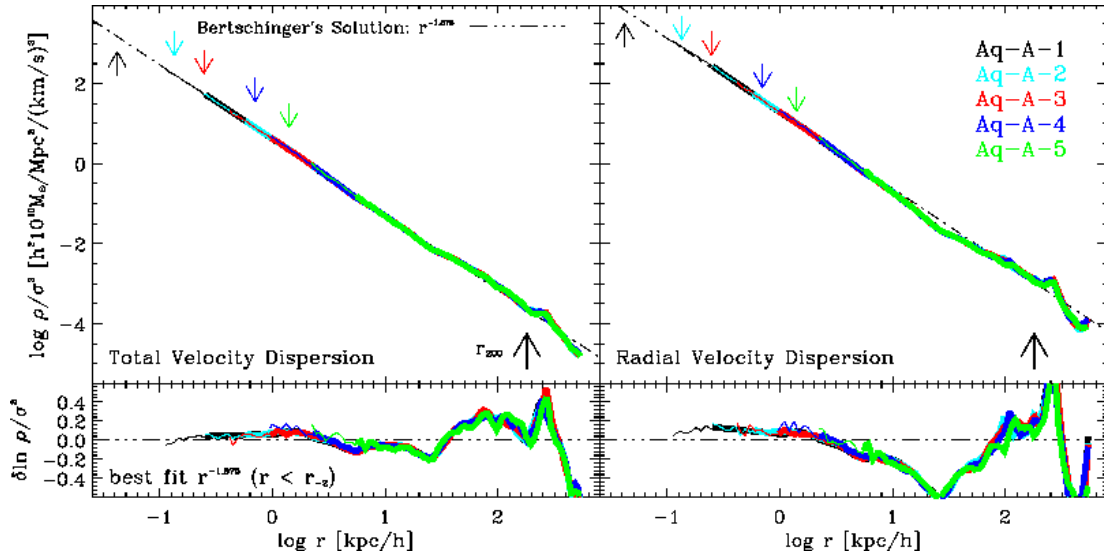
4.4 The phase-space density profile

The similarity in shape between the σ^2 and $r^2\rho$ profiles highlighted above suggests that there may be a simple scaling between densities and velocity dispersions in haloes. This is best appreciated by considering the quantity ρ/σ^3, which, for dimensional reasons, we

Figure 12. Local values of the logarithmic slope of the density profile plotted versus velocity anisotropy. The relation proposed by (Hansen & Moore 2006) is shown as a dashed line. Because the density profile steepens gradually from the centre outwards whereas the velocity anisotropy is non-monotonic, no simple relation between these two quantities is valid throughout the haloes. The Hansen & Moore formula approximates our results quite well in the inner regions, but large deviations may be seen outside r_{-2}, particularly at the largest radii where our haloes are approximately isotropic but their density profiles are steepest. Open circles correspond to $r_{conv}^{(1)} < r < r_{-2}$, filled circles to $r_{-2} < r < r_{200}$. Colours are as in Fig. 3.

shall call the pseudo-phase-space density, although it is important to realize that it is *not* the true coarse-grained phase-space density at the resolution of our simulations, or even the average of this quantity in spherical shells. For consistency with the rest of our analysis, we calculate ρ/σ^3 directly from the estimates of ρ and σ computed in concentric spherical shells.

Figure 13. Pseudo-phase-space density profiles for our Aq-A convergence series, estimated as ρ/σ^3, computed in concentric spherical shells. Arrows, line types and colours are as in Fig. 1. Note the remarkable power-law behaviour of this quantity, a result already noted by Taylor & Navarro (2001). The dot–dashed line is not a fit to the data, but rather the prediction of the similarity solution of Bertschinger (1985) for infall on to a point mass in an otherwise unperturbed Einstein–de Sitter universe, $\rho/\sigma^3 \propto r^{-1.875}$. This has been scaled to match Aq-A at $r < r_{-2}$. Residuals from the Bertschinger solution are shown in the bottom panels. Note that this power-law behaviour is most evident when the full three-dimensional velocity dispersion is used (left-hand panels). When only the radial velocity dispersion is used (right-hand panels), deviations from the Bertschinger solution are considerably larger.

Fig. 13 shows the ρ/σ^3 profile for our Aq-A convergence series. As noted by Taylor & Navarro (2001), the profile of this quantity is remarkably well approximated by a power law. More remarkable still is the fact that the power law is indistinguishable from that predicted by the similarity solution of Bertschinger (1985) for infall on to a point mass in an otherwise unperturbed Einstein–de Sitter universe, $\rho/\sigma^3 \propto r^{-1.875}$ (dot–dashed line in Fig. 13). This solution is spherically symmetric, involves purely radial motions, and is violently dynamically unstable, so its relevance to ΛCDM haloes is far from being clear. The residuals in the bottom panel of Fig. 13 are deviations from a Bertschinger law matched within the characteristic radius r_{-2}, where substructure bumps and wiggles are minimal.

Note that, although there is only *one free parameter* in this fit (the vertical scaling), the residuals do not exceed ~20 per cent *anywhere* within the virial radius, even though substructures add significant noise to the dynamical measurements in the outskirts of the halo. Interestingly, the residuals increase when σ_r, the velocity dispersion in radial motions, is used in place of the full three-dimensional rms velocity, σ, to estimate the 'phase-space density'. Thus, the $r^{-1.875}$ behaviour seems to concern the full kinetic energy content of each shell rather than just radial or tangential motions.

Fig. 14 shows that similar conclusions apply to the rest of the Aquarius haloes. Residuals from the Bertschinger law are small for all haloes, and are typically larger when the radial velocity dispersion is used. Note that there is some 'curvature' in the residual profiles, suggesting that a power law is a good, but perhaps not perfect, description of the radial dependence of ρ/σ^3. We are currently investigating the origin of this curvature and plan to report on it in a future paper (Ludlow et al., in preparation).

A power-law radial dependence is approximately preserved when σ_r is used, but the best-fitting value of the exponent differs systematically from -1.875. This may be seen in the bottom panels of Fig. 14, which show the residuals from the best-fitting $\rho/\sigma^3 \propto r^\chi$ law. The values of the best-fitting expo-

nent for both ρ/σ^3 and ρ/σ_r^3 (χ and χ_r, respectively) are listed in Table 2.

Perhaps the most important result from Fig. 14 is that there seems to be very little scatter between haloes when considering their ρ/σ^3 profiles. Take, for example, the case of halo Aq-E-2, which was a clear outlier in the density, velocity dispersion and anisotropy profiles. When considering ρ/σ^3, this halo is unremarkable and follows the Bertschinger law as closely as the others.

This shows that there is a sense in which ΛCDM haloes are nearly universal, but that universality does not extend to their density or velocity dispersion profiles separately, but rather only to their pseudo-phase-space density profile. This may appear a bold statement, and it certainly needs to be corroborated by future work, but it offers an intriguing perspective into the origin of the near-universal density profiles of haloes, the meaning of the Einasto shape parameter, α, and the provenance of their velocity dispersion structure. These issues deserve further investigation.

We end by noting that, although it is still not clear what leads to the power-law stratification of ρ/σ^3, these results may be used to place constraints on the structure of the central cusp, under the plausible (but admittedly unproven) assumption that the power-law behaviour of the phase-space density continues all the way to the centre. For example, Taylor & Navarro (2001) used this assumption to show that, for isotropic systems, a power-law pseudo-phase-space density implies an inner density cusp with $\rho \propto r^{-0.75}$. This is certainly consistent with the results shown in Fig. 7, which only exclude cusps steeper than $r^{-0.9\pm0.1}$. However, as we show in Fig. 5, the detailed profile which they derive for an isotropic halo with Bertschinger's power-law ρ/σ^3 profile is a significantly worse fit to our numerical data than the Einasto profile.

The power-law behaviour of the pseudo phase-space density has been confirmed by a number of authors and seems to be present even at early redshift (Vass et al. 2009). Interestingly, the average power-law exponent to the ρ/σ_r^3 profile is $\langle\chi_r\rangle \approx 1.97$, close to the 'critical' 1.94 required by Dehnen & McLaughlin (2005) to have
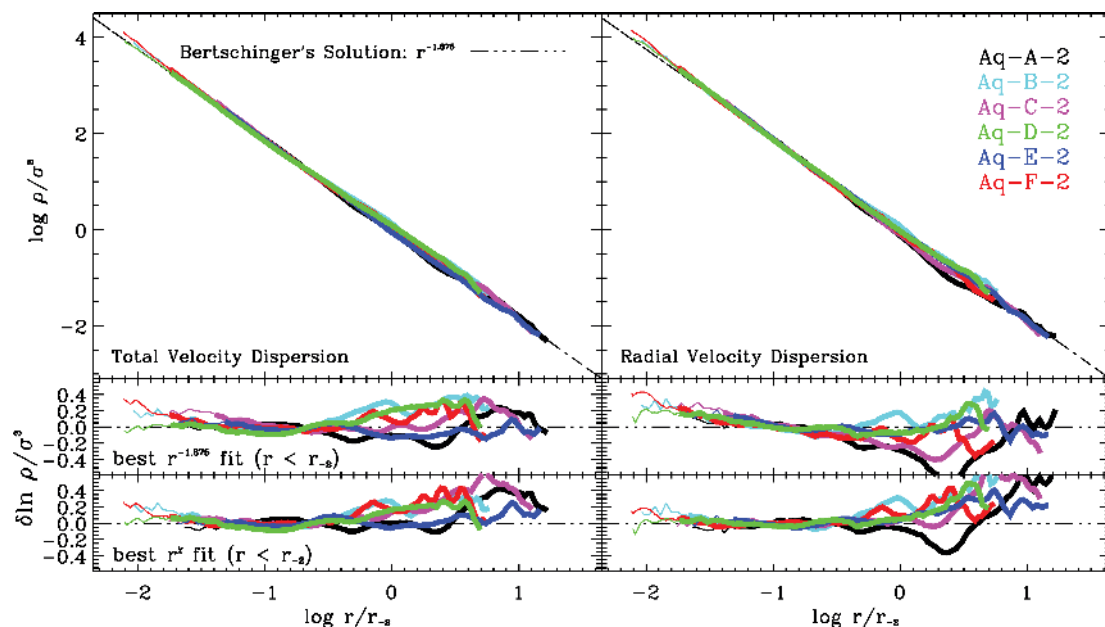
Figure 14. Pseudo-phase-space density profiles of all six level-2 Aquarius haloes. Radii have been scaled to r_{-2}, and the pseudo-phase-space densities to maximize agreement within r_{-2}. Note that for all six haloes these profiles are very well approximated by power laws with an exponent very close to that of the Bertschinger solution. All haloes, including those that were outliers in the density, velocity dispersion and anisotropy profiles, are almost indistinguishable in this plot. Deviations from the Bertschinger law are typically more pronounced when radial velocity dispersion is used instead of the full three-dimensional velocity dispersion. Residuals from the best-fitting power laws, $\rho/\sigma^3 \propto r^\chi$, are shown in the bottom panels. The values of χ are listed for each halo in Table 2.

a dynamical model that is well behaved at all radii. Simulations of even larger dynamic range seem required in order to explore the true asymptotic inner behaviour of the dynamical profile of a halo, if indeed there is any such asymptote.

5 SUMMARY

We have analysed density, velocity dispersion, anisotropy and pseudo-phase-space density profiles at redshift zero for simulated haloes from the *Aquarius Project*. This is a set of six galaxy-sized haloes whose formation and evolution have been simulated at a variety of resolutions in their proper ΛCDM context. The set includes the largest simulation of this kind reported so far; an ∼4.4 billion particle simulation in which the final halo has 1.1 billion particles within its virial radius, r_{200}. The set also includes simulations of all six haloes with 100–200 million particles within the virial radius, as well as a comprehensive numerical convergence study for the largest system. Our analysis confirms a number of results claimed by earlier work, and clarifies a few issues where conflicting claims may be found in the recent literature. Our main conclusions are as follows.

(i) Density profiles deviate slightly but significantly from the NFW model, and are approximated well by a fitting formula where the logarithmic slope is a power law of radius: the Einasto profile (equation 4). The steeply cusped profile of Moore et al. (1999b) is a poor fit to the structure of our six haloes.

(ii) We find convincing evidence that the shape parameter of the Einasto formula varies from halo to halo at given mass (see Table 2). This complements the earlier conclusion of Merritt et al. (2006), Gao et al. (2008) and Hayashi & White (2008) that its mean value varies systematically with halo mass. Together these results imply that the density profiles of ΛCDM haloes are not strictly self-similar: different haloes cannot be rescaled to look alike. This lack of similarity extends to the kinematic structure, as measured by the velocity dispersion and anisotropy profiles.

(iii) Intriguingly, departures from similarity are minimized when analysing a pseudo-phase-space density profile defined as ρ/σ^3. This suggests a limited sense in which ΛCDM haloes are indeed nearly 'universal'. The pseudo-phase-space density profiles are very well approximated by $\rho/\sigma^3 \propto r^{-1.875}$, the power law predicted by Bertschinger's similarity solution for infall on to a point mass in an otherwise unperturbed Einstein–de Sitter universe. This simple law has only *one* scaling parameter and no shape parameters, yet it approximates, for over six decades, the ρ/σ^3 profiles to better than 20–30 per cent, all the way from the innermost resolved point to the virial radius. The power-law description is, however, not perfect, and further work designed to understand better its origin and limitations seems warranted.

(iv) Density profiles become monotonically shallower inwards, down to the innermost resolved point, with no indication that they approach power-law behaviour. The innermost slope we measure is slightly shallower than −1, a result supported by estimates of the maximum possible asymptotic inner slope.

(v) These results convincingly rule out recent claims that typical ΛCDM haloes may have asymptotic central cusps as steep as $r^{-1.2}$ (Diemand et al. 2004, 2005, 2008). Shallower cusps, such as the asymptotic $r^{-0.75}$ behaviour predicted by the model of Taylor & Navarro (2001), cannot yet be excluded. These results should discourage further work assuming CDM cusps steeper than r^{-1} except possibly around central black holes.

(vi) Velocity anisotropy does not depend monotonically on radius beyond r_{-2}. Haloes are roughly isotropic near the centre, are dominated by radial motions at intermediate radii, but become more isotropic again as the virial radius is approached. This behaviour does not appear to be driven by the presence of substructure. Given that the slope of the density profile does increase monotonically with radius, this implies that no simple relation between anisotropy

and slope can hold throughout a halo. The relation recently proposed by Hansen & Moore (2006) works reasonably well in the inner regions ($r < r_{-2}$), but fails at larger radii.

The main aim of the *Aquarius Project* is to provide reliable theoretical predictions for the structure and formation history of dark matter haloes like that surrounding the Milky Way down to radii of the order of 100 pc. This permits direct comparisons with a number of observations with minimal extrapolation, and it helps to design new observational strategies aimed at testing the CDM paradigm on these very non-linear scales.

We recognize, however, that many of these tests and predictions will apply to regions where baryons play an important dynamical role. Our numerical work provides robust results for the limiting but unrealistic case of *pure dark matter* haloes, and these will undoubtedly be modified in non-trivial ways by the presence of baryons. Providing a full account of the coupled structure of the CDM *and* baryonic components in galaxies like our own is clearly the next major computational challenge, and it is likely to exercise us for some time to come.

REFERENCES

Allgood B., Flores R. A., Primack J. R., Kravtsov A. V., Wechsler R. H., Faltenbacher A., Bullock J. S., 2006, MNRAS, 367, 1781
Bertschinger E., 1985, ApJS, 58, 39
Dehnen W., McLaughlin D. E., 2005, MNRAS, 363, 1057
Diemand J., Moore B., Stadel J., 2004, MNRAS, 353, 624
Diemand J., Zemp M., Moore B., Stadel J., Carollo C. M., 2005, MNRAS, 364, 665
Diemand J., Kuhlen M., Madau P., 2007, ApJ, 657, 262
Diemand J., Kuhlen M., Madau P., Zemp M., Moore B., Potter B., Stadel J., 2008, Nat, 454, 735
Einasto J., 1965, Trudy Inst. Astroz. Alma-Ata, 51, 87
Eke V. R., Cole S., Frenk C. S., 1996, MNRAS, 282, 263
Frenk C. S., White S. D. M., Davis M., Efstathiou G., 1988, ApJ, 327, 507
Fukushige T., Makino J., 2001, ApJ, 557, 533
Gao L., White S. D. M., Jenkins A., Stoehr F., Springel V., 2004, MNRAS, 355, 819
Gao L., Navarro J. F., Cole S., Frenk C. S., White S. D. M., Springel V., Jenkins A., Neto A. F., 2008, MNRAS, 387, 536
Ghigna S., Moore B., Governato F., Lake G., Quinn T., Stadel J., 2000, ApJ, 544, 616
Graham A. W., Merritt D., Moore B., Diemand J., Terzic B., 2006, AJ, 132, 2701
Hansen S. H., Moore B., 2006, New Astron., 11, 333
Hayashi E., White S. D. M., 2008, MNRAS, 388, 2
Hayashi E., Navarro J. F., Springel V., 2007, MNRAS, 377, 50
Henry J. P., Evrard A. E., Hoekstra H., Babul A., Mahdavi A., 2009, ApJ, 691, 1307
Jing Y. P., Suto Y., 2002, ApJ, 574, 538
Klypin A., Kravtsov A. V., Valenzuela O., Prada F., 1999, ApJ, 522, 82
Komatsu E. et al., 2009, ApJS, 180, 330
Kuhlen M., Diemand J., Madau P., 2008, ApJ, 686, 262
Merritt D., Navarro J. F., Ludlow A., Jenkins A., 2005, ApJ, 624, L85
Merritt D., Graham A. W., Moore B., Diemand J., Terzić B., 2006, AJ, 132, 2685
Moore B., Ghigna S., Governato F., Lake G., Quinn T., Stadel J., Tozzi P., 1999a, ApJ, 524, L19
Moore B., Quinn T., Governato F., Stadel J., Lake G., 1999b, MNRAS, 310, 1147 (M99)
Navarro J. F., Frenk C. S., White S. D. M., 1996, ApJ, 462, 563 (NFW)
Navarro J. F., Frenk C. S., White S. D. M., 1997, ApJ, 490, 493 (NFW)
Navarro J. F. et al., 2004, MNRAS, 349, 1039
Power C., Navarro J. F., Jenkins A., Frenk C. S., White S. D. M., Springel V., Stadel J., Quinn T., 2003, MNRAS, 338, 14 (P03)
Prugniel P., Simien F., 1997, A&A, 321, 111
Sersic J. L., 1968, Atlas de Galaxias Australes, Observatorio Astronomico, Cordoba, Argentina
Spergel D. N. et al., 2003, ApJS, 148, 175
Springel V., 2005, MNRAS, 364, 1105
Springel V., Yoshida N., White S. D. M., 2001, New Astron., 6, 79
Springel V. et al., 2005, Nat, 435, 629
Springel V. et al., 2008a, MNRAS, 391, 1685
Springel V. et al., 2008b, Nat, 456, 73
Stadel J., Potter D., Moore B., Diemand J., Madau P., Zemp M., Kuhlen M., Quilis V., 2009, MNRAS, 398, L21
Stoehr F., 2006, MNRAS, 365, 147
Stoehr F., White S. D. M., Springel V., Tormen G., Yoshida N., 2003, MNRAS, 345, 1313
Taylor J. E., Navarro J. F., 2001, ApJ, 563, 483
Vass I. M., Valluri M., Kravtsov A. V., Kazantzidis S., 2009, MNRAS, 395, 1225
Vogelsberger M. et al., 2009, MNRAS, 395, 797
White S. D. M., 1996, in Schaefer R., Silk J., Spiro M., Zinn-Justin J., eds, Cosmology and Large-Scale Structure. Elsevier, Dordrecht, p. 349

This paper has been typeset from a TEX/LATEX file prepared by the author.